BNL-209514-2018-JAAM

Control of magnetic anisotropy by orbital hybridization with charge transfer in (La0.67Sr0.33MnO3)(n)/(SrTiO3)(n) superlattice

B. Zhang, L. Wu

To be published in "NPG ASIA MATERIALS"

September 2018

Condensed Matter Physics and Materials Science Department

Brookhaven National Laboratory

U.S. Department of Energy

USDOE Office of Science (SC), Basic Energy Sciences (BES) (SC-22)

Notice: This manuscript has been authored by employees of Brookhaven Science Associates, LLC under Contract No. DE-SC0012704 with the U.S. Department of Energy. The publisher by accepting the manuscript for publication acknowledges that the United States Government retains a non-exclusive, paid-up, irrevocable, world-wide license to publish or reproduce the published form of this manuscript, or allow others to do so, for United States Government purposes.

DISCLAIMER

This report was prepared as an account of work sponsored by an agency of the United States Government. Neither the United States Government nor any agency thereof, nor any of their employees, nor any of their contractors, subcontractors, or their employees, makes any warranty, express or implied, or assumes any legal liability or responsibility for the accuracy, completeness, or any third party's use or the results of such use of any information, apparatus, product, or process disclosed, or represents that its use would not infringe privately owned rights. Reference herein to any specific commercial product, process, or service by trade name, trademark, manufacturer, or otherwise, does not necessarily constitute or imply its endorsement, recommendation, or favoring by the United States Government or any agency thereof or its contractors or subcontractors. The views and opinions of authors expressed herein do not necessarily state or reflect those of the United States Government or any agency thereof.

Control of magnetic anisotropy by orbital hybridization with charge transfer in $(La_{0.67}Sr_{0.33}MnO_3)_n/(SrTiO_3)_n$ superlattice

Bangmin Zhang,[‡,//] Lijun Wu,[Δ,//] Jincheng Zheng,[Δ,Λ] Ping Yang,[□] Xiaojiang Yu,[□] Jun Ding,[‡] Steve M. Heald,[◊] R. A. Rosenberg,[◊] T. Venkatesan,[⊥,▽,§,¥] Jingsheng Chen,[‡] Cheng-Jun Sun,[◊,] Yimei Zhu,[Δ,*] and Gan Moog Chow[‡,*]*

[‡]Department of Materials Science & Engineering, National University of Singapore, 117576, Singapore.

[Δ]Condensed Matter Physics & Materials Science Division, Brookhaven National Laboratory, Upton, New York 11973, USA.

[Λ]Department of Physics, Xiamen University, Xiamen 361005, People's Republic of China.

[□]Singapore Synchrotron Light Source (SSLS), National University of Singapore, 5 Research Link, 117603 Singapore.

[◊]Advanced Photon Source, Argonne National Laboratory, Argonne, IL 60439, USA.

[⊥]NUSNNI-Nanocore, National University of Singapore, 117411, Singapore.

[▽]Department of Physics, National University of Singapore, 117542, Singapore.

[§]Department of Electrical & Computer Engineering, National University of Singapore, 117576, Singapore.

[¥]Department of Integrative Science and Engineering, National University of Singapore, 117xxx, Singapore.

*Corresponding authors: cjsun@aps.anl.gov; zhu@bnl.gov; msecgm@nus.edu.sg

Abstract:

The asymmetry of chemical nature at the hetero-structural interface offers a unique opportunity to design the needed electronic structure by controlling charge transfer and orbital hybridization across the interface. However, control of hetero-interface is still a daunting task. Here, we report the modulation of interfacial coupling of $(SrTiO_3)_n/(La_{0.67}Sr_{0.33}MnO_3)_n$ superlattices by manipulating the periodic thickness with *n* unit cells of $SrTiO_3$ and *n* unit cells $La_{0.67}Sr_{0.33}MnO_3$. The easy axis of magnetic anisotropy rotates from in-plane (*n* = 10) to out-of-plane (*n* = 2) orientation at 150 K. Transmission electron microscopy reveals enlarged tetragonal ratio > 1 with broken of volume conservation around $(SrTiO_3)_n/(La_{0.67}Sr_{0.33}MnO_3)_n$ interface, and electronic charge transfer from Mn to Ti 3*d* orbitals across the interface. Orbital hybridization across the interface results in preferred occupancy of $3\boldsymbol{d}_{3z^2-r^2}$ orbital at the interface, which induces a stronger electronic hopping integral along the out-of-plane direction and corresponding perpendicular magnetic easy axis for *n* = 2. We demonstrate that interfacial coupling-induced orbital hybridization in superlattices of strongly correlated oxides can be a promising approach to tailor electronic and magnetic properties for applications such as magnetic tunnel junctions.

Main text:

The asymmetry at hetero-structural interface of 3*d* transitional metal ABO_3 oxides, including the mismatch of lattice constant, oxygen octahedral rotation and distortion, and chemical environment, has profound influences on spin and orbital coupling, yielding interesting phenomena, such as enhanced ordering temperature, magnetism of superconductor and orbital reconstruction.[1-5] Coupling of interfacial crystal structure[6-12] leads to new properties, for example, film-thickness dependent interfacial ferromagnetic-polaronic insulator in $Pr_{0.67}Sr_{0.33}O_3/SrTiO_3$[13], spontaneous deep polarization[9] in $SrTiO_3$ near the $La_{2/3}Sr_{1/3}MnO_3/SrTiO_3$ interface, rotation of magnetic easy axis of $La_{2/3}Sr_{1/3}MnO_3$[14] and $SrRuO_3$[15] thin film. In strongly correlated system, the properties of transition metal oxides are sensitive to the electronic structure, especially the occupation of 3*d* orbitals.[4] The electronic structure can be manipulated by doping with different covalent ions,[16] hydraulic pressure,[17] and external electric bias.[18-19] Control of electronic structure may also be exploited using chemical asymmetry at hetero-structure interface to induce electronic charge transfer and orbital hybridization across the interface,[20-22] such as in $(YBa_2Cu_3O_7)/(PrBa_2Cu_3O_7)$ superlattice.[20]

The short-range charge transfer is constrained to several unit cells (UC) within the proximity of the interface,[22-24] as illustrated by the probability of charge transfer in Fig. 1**A**-1**B**. Artificial superlattices of ABO_3 with multiple interfaces provide a viable way to manipulate the intensity of interfacial coupling and corresponding properties. $La_{0.67}Sr_{0.33}MnO_3$ (LSMO) has a pseudo-cubic lattice of 3.880 Å, high Curie temperature and high spin polarization.[25] $SrTiO_3$ (STO) is cubic[26-27] with lattice constant ~ 3.905 Å that is close to that of LSMO. Some properties of STO/LSMO systems, such as insulator-metal transition temperature,[28] magnetoelastic effect,[29] and octahedral rotation[30] have been investigated. The difference in electrochemical potential[22] at the STO/LSMO interface due to mismatch of chemical environment may drive the electronic

charge transfer from Mn to Ti sites, as illustrated in Fig. 1**B**. To date, electronic charge transfer and related properties at LSMO/STO interfaces remain an open area. Increased number of STO/LSMO interfaces may enhance the probability of short-range charge transfer, which offers a method to study the effect of charge transfer.

In this work, we report the manipulation of interfacial electronic properties and corresponding magnetic anisotropy in $[(SrTiO_3)_n/(La_{0.67}Sr_{0.33}MnO_3)_n]_m$ superlattices (SL) with different periodic thickness (*n* UC LSMO and *n* UC STO in one period, referred to SL*n* hereafter. The total superlattice thickness was kept at 2n×m ~ 120 UC). The periodic thickness of SL*n* was systematically changed to obtain different numbers of STO/LSMO interfaces, as illustrated in Fig. 1**A**. The magnetic anisotropy was measured by a superconducting quantum interference device (SQUID) at 150 K and 10 K. At 150K, the magnetic easy axis of SL10 (in-plane) is clearly different from SL2 (out-of-plane), as shown in Fig. 1**C**-1**D**. The element-specific magnetic information was revealed using X-ray magnetic circular dichroism (XMCD). The difference in magnetic easy axis of different samples is further confirmed by angular-dependent Mn $\boldsymbol{L}_{3,2}$ edge XMCD in Fig. **S1.** The contribution from Ti sites to the total magnetic moment is insignificant as calculated by sum rules[31] from Ti $\boldsymbol{L}_{3,2}$ XMCD. Hence the discussion of magnetic properties in this work will mainly focus on the contribution from Mn sites hereafter. For details on angular-dependent XMCD, see Figs. **S1-S2**.

The effective anisotropy may be viewed as the sum of contributions favoring in-plane orientation ($H_{//}$) and that favoring out-of-plane orientation ($H_{\perp}$), as illustrated in the inset of Fig. 1**C**-1**D**. The effective anisotropy field[32] could be decoupled as $H_{eff} = H_i + H_b - H_d$, including constant bulk term $\boldsymbol{H}_b$ and demagnetization term $\boldsymbol{H}_d$ favoring in-plane direction, and interfacial contribution $\boldsymbol{H}_i$ favoring out-of-plane direction. Compared to the bulk, multiple interfaces in

superlattice render $\boldsymbol{H}_d$ and $\boldsymbol{H}_i$ non-trivial. The calculated interfacial contribution $\boldsymbol{H}_i$ (Fig. 1**E**) increases with decreasing *n*. The positive value of $\boldsymbol{H}$ is defined to denote the easy axis normal to the film plane and a negative value means the easy axis in the film plane. The change of the interfacial contribution $\boldsymbol{H}_i$ is responsible for the change of easy axis as a function of periodic thickness of the superlattices. Analysis of the magnetic anisotropy at 10 K (Figs. **S3-S4**) shows in-plane magnetic easy axis for all samples. Although the total effective magnetic anisotropy at 10 K does not switch due to the strong demagnetization contribution $\boldsymbol{H}_d$, the interfacial contribution $\boldsymbol{H}_i$ shows similar trend as that at 150 K. Hence, the effect of periodic thickness on interfacial term $\boldsymbol{H}_i$ exists in a wide temperature range.

For the mechanisms of the interfacial term $\boldsymbol{H}_i$, one possible reason is the oxygen octahedral rotation coupling cross the interface. The anisotropy of $La_{2/3}Sr_{1/3}MnO_3$ film (several UC) was demonstrated to switch between the in-plane $\boldsymbol{a}$ and $\boldsymbol{b}$ axes by inserting a $SrTiO_3$ buffer layer between the film and a $NdGaO_3$ substrate,[14] which affected oxygen octahedral rotation at the interface and the corresponding hopping integral ($\boldsymbol{t}$) between neighboring sites. Similarly, a $Ca_{0.5}Sr_{0.5}TiO_3$ buffer layer was inserted between the $SrRuO_3$ film and the $GdScO_3$ substrate[15] to modulate the bond angle $\theta_{Ru\text{-}O\text{-}Ru}$ or the RuO_6 octahedral distortions, which could switch the magnetic easy axis from in-plane to out-of-plane directions. The volume-averaged x-ray half-integer diffraction[33-35] was used to measure the MnO_6 rotation in order to retrieve the bond angle information in this work (Fig. **S5)**. There is a significant difference in Mn-O bond angle and bond length in SL10 for the in-plane and out-of-plane directions. In SL2, the bond lengths of both directions are similar, yet the bond angles are different. The larger in-plane bond angle for SL2 (Fig. **S5B**) suggests higher in-plane hopping integral which favors in-plane magnetic easy

axis instead of the observed out-of-plane direction. It is therefore reasonable to consider other factors that are responsible for the observed magnetic anisotropy.

High-angle annular dark field (HAADF) imaging of scanning transmission electron microscopy (STEM), high resolution TEM (HRTEM) imaging and select area electron diffraction (SAED) were used to probe the local information at the LSMO/STO interfaces for n = 2, 6, 10, as shown in Fig. 2**A**-2**C** and Fig. **S6**-**S9**. The STO substrate was treated with a TiO_2 termination layer before deposition, and an atomically-flat interface between LSMO/STO existed in these samples. The film is perfectly aligned with the STO substrate horizontally, and the substrate is at the left side of image as shown in Fig. **S6**. By refining the peak positions, we obtain the plane spacing of two successive (001) La/SrO (or SrO) planes along out-of-plane direction (hereafter denoted as c_{int}), as shown in Fig. 2**A** for SL6 and Fig. **S7** for SL10. For SL6, the c_{int} shows an oscillating pattern with maximum value at left STO/LSMO interface of each LSMO superlayer, larger than 3.905 Å, and with minimum at right LSMO/STO interface for each LSMO superlayer. Similar behavior is observed in SL10 (Fig. **S7)**. The oscillation pattern of c_{int} in the film is confirmed by geometry phase analysis (GPA)[36-37] from HRTEM image (the second row in Fig. 2**B** and Fig. **S8A**). There is basically no changes of in-plane lattice (the third row in Fig. 2B) over the whole images except some random changes caused by the image noise. For SL2, there is no obvious pattern (Fig. 2**C** and Fig. **S8B**), but c_{int} of the film is slightly larger than that of the substrate STO. The (002) peak (blue line in Fig. **S9E**) from the diffractogram of SL2 film shift to left with respect to that of the substrate (red line), confirming that the c_{int} of SL2 film is larger than that of STO substrate. The SAED from the SL2 film determines that the lattice parameters of SL2 film are a = 3.905 Å and c_{int} = 3.911 Å, which is consistent with the trend of XRD results. The shoulder at right side of (002) X-ray diffraction reflection, corresponding to

the film, is quite clear for SL6-SL10, but almost disappears after SL4 (Fig. **S10**). Peak position refinement reveals that the out-of-plane lattice constant increases with the decrease of *n* for SL*n*. Similar enlarged tetragonal ratio has been reported in other heterostructural interface,[38-39] and affects the materials properties, such as the electronic structure. In addition, the Mn displacement from body center of pseudo-cubic UC is observed**,** the effect of which is discussed in **S11**.

From above discussion, the enlarged $c_{int}/a > 1$ around LSMO/STO interface may induce the perpendicular anisotropy in SL2 due to the interfacial coupling. However, the broken of volume conservation indicates that the conventional misfit-strain is not enough to explain the phenomenon, and additional factor should be addressed. In strongly correlated 3*d* oxide, the crystal structure and electronic structure are highly correlated. Then the electronic charge distribution was examined and verified by Ti ***L*** edge electron energy loss spectroscopy (EELS). The Ti ***L*** edge EELS[40-41] at different positions in SL6 and SL2 are presented in Fig. 2**D**, and the analyzed results are summarized in the lower part of Fig. 2**A** and 2**C**, respectively. For SL6, the chemical valence of Ti at LSMO/STO interface ~ 3.78 decreases compared to that at the center of STO layer ~ 3.97, suggesting that extra electrons are accepted by the Ti 3*d* orbitals at the STO/LSMO interface. Similar trend occurs in SL10 (Fig. **S7**). The average chemical valence of Ti is ~ 3.75 in SL2 because each STO unit cell locates at the LSMO/STO interface. There is no clear trend of chemical valence of Mn[42-43], as revealed in Fig. **S12**. However, comparison of the curve shape (rather than the peak position) of X-ray absorption between simulated and measured Mn ***L*** edge XAS, suggests higher Mn chemical valence than 3.3. See **S12** for more details on Mn XAS simulation. Combing above discussion, the charge transfer from Mn to Ti 3*d* orbitals is suggested.

The properties of manganite are sensitive to the 3*d* orbital occupancy, and the Mn *L* edge X-ray linear dichroism (XLD) was measured to study the electronic configuration, as shown in Fig. 3**A**-3**B**. The difference of two X-ray absorption spectra shows the difference of occupancy in two e_g orbitals. The gradual decrease of intensity of the feature at ~ 640 eV is due to the gradual increase of relative occupancy of $3\boldsymbol{d}_{3z^2-r^2}$ orbitals with decreasing *n*, as shown in Fig. 3**B**. Compared with previous reports[44-45], the XLD of SL2 confirms the preferred occupancy of $3\boldsymbol{d}_{3z^2-r^2}$ orbitals. The resultant depletion of the $3\boldsymbol{d}_{x^2-y^2}$ orbitals leads to weakening of ferromagnetic double-exchange interaction[45] and low paramagnetic-ferromagnetic phase transition temperature in SL2, as shown in Fig. **S4**. The relative occupancy of $3\boldsymbol{d}_{3z^2-r^2}$ orbitals has obvious effect on the angular-dependent magnetoresistance (AMR) at 10 K. In the AMR measurement, the applied magnetic field is rotated from in-plane to out-of-plane directions, and the in-plane current is always perpendicular to the applied magnetic field as shown in the inset of Fig. 3**C**. At 10 K, all films show in-plane magnetic anisotropy (Fig. **S3**). Normally the minimum resistance should occur when the applied magnetic field is in the film plane. However, with increasing magnetic field from 1 kOe to 80 kOe, the minimum resistance point of SL3 changes from in-plane to the out-of-plane directions (Fig. 3**C**). This phenomenon is related to orbital reconstruction[46] with electronic charge transfer across the STO/LSMO interface, especially the $3\boldsymbol{d}_{3z^2-r^2}$ orbital occupancy. When magnetic field are applied in the film plane, the $3\boldsymbol{d}_{3z^2-r^2}$ band gets flatter at Fermi level due to the spin-orbital coupling, and results in a larger resistivity compared to that with perpendicular magnetic field. Fig. 3**D** shows that AMR effect is largest for SL3 and decreases with increasing *n*. Although the resistance of SL2 exceeds the measurement capability at low temperature, as shown in Fig. **S4**, the trend of AMR suggest that effect of orbital

reconstruction at STO/LSMO interface increases with decreasing *n* (enhanced interfacial coupling).

Several reports[36,44] have addressed the origin of the preferred occupancy of $3\boldsymbol{d}_{3z^2-r^2}$ at the heterostructure interface, invoking arguments such as the interfacial symmetry breaking and new crystal structure phase. Based on the existence of the electronic charge transfer and AMR at low temperature, a possible mechanism due to the orbital hybridization across the interface[47-48] is proposed as shown in Fig. 4**A**. From the perspective of molecular orbitals, the formed interfacial bonding orbital lowers the energy of 3*d* orbitals, favoring the occupancy of the $3\boldsymbol{d}_{3z^2-r^2}$ orbital due to a large spatial overlap. When this interfacial orbital forms, electronegativity of the interfacial bonds may facilitate the charge transfer between Mn and Ti 3*d* orbitals, and then affects the bond length and bond angle. Due to the correlation between the crystal structure and the electronic structure in 3*d* oxides, the preferred $3\boldsymbol{d}_{3z^2-r^2}$ orbital occupancy would enlarge the out-of-plane c_{int} to lower the total energy, supported by the enlarged $c_{\mathrm{int}}/a > 1$ around the left LSMO/STO interface of each LSMO layer (Fig. 2**B**) from STEM and XRD in Fig. **S10**. This oscillating pattern of c_{int} for SL6 and SL10 (Fig. **2A** and Fig. **S7**) indicates strong coupling across the interface, which could be understood as below: taking LSMO layer as example, from the left to right the 1st UC LSMO has the strongest coupling with its left STO layer, thus has large c_{int}. Then the coupling with STO layer decreases with increasing distance from the interface, and the value of c_{int} of LSMO tends to decrease and reaches its minimum value at the right interface of LSMO layer. The following 1st STO UC is affected by the LSMO layer and its c_{int} has a minimum value. With increasing distance, the coupling effect from LSMO layer deteriorates and the value of c_{int} of STO increases until the next interface. At both left and right interfaces of LSMO layer the charge transfer occurs, which induces the enlarged out-of-plane c_{int} and lowered

Ti chemical valence around LSMO/STO interface. However, careful examination shows that the chemical valence asymmetry occurs in SL6: taking LSMO layer as example for convenience, Ti at the left STO/LSMO interface has lower chemical valence than that at right LSMO/STO interface. The atomic structure is -SrO-TiO_2-La/SrO-MnO_2- at the left interface, and -MnO_2-SrO-TiO_2-SrO at the right interface. Then the TiO_2 atomic layer at the left interface directly contacts with La^{3+} ions, which would lower the effective chemical valence of Ti ions. This difference of chemical environment may contribute to the asymmetry of chemical valence, as well as observed c-lattice oscillation, the effect of which guarantees further investigation.

The preferred $3\boldsymbol{d}_{3z^2\text{-}r^2}$ orbital occupancy itself has no direct connection[14] with the perpendicular easy axis in SL2, but the mechanism of the switching of magnetic anisotropy could be addressed as below based on the electronic hopping integral. A tight-binding Hamiltonian[14] of LSMO ultrathin films: $\sum_R t_{\alpha\beta}(R)e^{iK\bullet R} + \left(\frac{\lambda}{2}\right)\sigma(\theta,\varphi) + \xi L \bullet S$ was proposed to explain the magnetic anisotropy energy (MAE) according to density functional theory. $t_{\alpha\beta}(R)$ represents the hopping integral from orbital α at the original site to orbital β at site **R**. The structural change mainly affects $t_{\alpha\beta}(R)$, which in turn leads to the change of magnetic anisotropy. In magnetic materials, a high hopping integral is favored along the magnetic easy axis. In our current work, the hopping integral along the in-plane t_{in} and out-of-plane t_{out} direction, illustrated in Fig. 4**B**, may shed light on the origin of perpendicular magnetic anisotropy in SL2. The relative intensity of the hopping integral correlates to the detailed shape of the polarization dependent Mn ***K*** edge X-ray Absorption Near Edge Structure (XANES)[35, 49-50] as shown in Fig. 4**C-4E** and Fig. **S13**. After X-ray absorption, the electronic configuration of MnO_6 octahedron in B1 status is proportional to the hopping integral, and then the relative ratio of B1 in polarization dependent XANES is used to characterize the in-plane and out-of-plane

hopping integral: The higher intensity ratio ($\Lambda_{//}$= I_{B1}/I_{B2}) in the parallel measurement with the polarization vector (***E*** vector of X-ray) parallel to the film plane suggested higher out-of-plane hopping integral t_{out}.[35, 49-50] For SL2, the out-of-plane hopping integral t_{out} is higher than in-plane hopping integral t_{in} in Fig. **4D**, induced by the enhanced $3\boldsymbol{d}_{3z^2-r^2}$ orbital occupancy, which would favor the out-of-plane magnetic anisotropy based on the tight-binding Hamiltonian. In addition, with the decrease of *n*, $\Lambda_{//}$ increases and the $\Lambda_{//}/\Lambda_{\perp}$ ratio also increases as shown in Fig. 4**E**, indicating that the difference of electronic hopping integral along in-plane and out-of-plane directions increases for decreasing *n*. This is consistent with the trend of $\boldsymbol{H}_{\mathrm{i}}$ with different periodic thickness *n*.

In summary, the interfacial properties in $(STO)_n/(LSMO)_n$ superlattice has been studied. The variation of periodic thickness in superlattices affects the interfacial atomic arrangement and induced charge transfer and orbital hybridization. Increasing the number of interfaces therefore enhances the orbital hybridization, as evident in the interfacial electronic charge transfer from Mn 3*d* and Ti 3*d* orbitals and resultant out-of-plane magnetic easy axis (SL2). This work demonstrates a promising approach of the use of superlattices to manipulate the interfacial orbital hybridization and corresponding electronic charge transfer. The designed control of interface-induced properties of strongly correlated oxides have significant potentials in magneto-electronic devices.

Materials and Methods

Sample fabrication: $La_{0.67}Sr_{0.33}MnO_3/SrTiO_3$ films with different thicknesses were grown on (001) $SrTiO_3$ (STO) substrate by pulsed laser deposition equipped with reflection high-energy electron diffraction (RHEED) to monitor the thickness, at 100 mTorr oxygen pressure at a substrate temperature of 780°C. After deposition, the sample was cooled down at 15°C /min in a 200 mTorr oxygen atmosphere. The energy density of the 248 nm KrF excimer laser beam on target was 1.5 J/cm^2 at a pulse frequency of 2 Hz.

Transport and magnetic properties: The magnetic properties were measured by a superconducting quantum interference device (SQUID), and the transport properties were measured by the Physical Property Measurement System (PPMS) using linear four point probe. During measurement, the magnetic field was applied along the in-plane [100] direction.

X-ray measurement: The crystallographic texture of films at room temperature was studied using a four-circle diffractometer at the Singapore Synchrotron Light Source (SSLS), with x-ray wavelength equal to Cu $K_{\alpha 1}$ radiation.

The X-ray absorption near edge structure (XANES) measurements were carried out using linear polarized X-rays at the undulator beamline 20-ID-B of the Advanced Photon Source (APS), Argonne National Laboratory (ANL), USA. The Si (111) monochromator with resolution $\delta \boldsymbol{E}/\boldsymbol{E}$ = 1.3 x 10^{-4} was used. The XANES was collected in fluorescence mode using a 12-element Ge solid-state detector. A Mn metal foil, placed to intercept a scattered beam, was used as an online check of the monochromator energy calibration. In order to get reliable information, each XANES curve is averaged results of five measurements with total counts more than one million.

The magnetic moment was measured using superconducting quantum interference device (SQUID) and X-ray magnetic circular dichroism (XMCD). The XMCD at the $\boldsymbol{L}_{3,2}$ edges of Mn

were measured with an applied in-plane magnetic field of 0.5 T, which were conducted at beamline 4-ID-C at the APS in ANL using total electron mode for data collection at 150 K.

The XANES spectra and XMCD difference spectra were simulated using the FDMNES code.[51] The final states of electron in the cluster with radius of 6 angstrom were calculated using the multiple-scattering approach with spin-orbit coupling included. To account for the core-hole lifetime, the calculated XANES and XMCD spectrum at the ***L*** edges of Mn were convoluted with a Lorentzian function. In addition, to account for the experimental resolution and scaling of the spectra, a complementary convolution with a Gaussian function with typical broadening parameters σ=1.0 eV was performed. The spectra of Mn with various chemical valences are normalized for easy comparison.

Transmission electron microscopy: SAED, HRTEM, STEM-HAADF and EELS spectrum imaging were performed using the double aberration-corrected JEOL-ARM200CF microscope with a cold-field emission gun and operated at 200 kV, at Brookhaven National Laboratory, USA. The microscope is equipped with JEOL and Gatan HAADF detectors for incoherent HAADF (Z-contrast) imaging, Gatan GIF Quantum ER Energy Filter with dual EELS for EELS. The cross-section TEM samples were prepared by focused ion beam (FIB) followed by gentle ion-milling at low operating voltages. The STEM-HAADF images were acquired with condense aperture of 21.2 mrad and collection angle of 67-275 mrad.

Supporting Information. Additional experimental and calculation details, figures, and tables. This material is available free of charge via the Internet.

Author Contributions (//): B.Z. and L.W. contributed equally.

Corresponding Author: * cjsun@aps.anl.gov; zhu@bnl.gov; msecgm@nus.edu.sg

Notes: The authors declare no competing financial interest.

Acknowledgements

The research is supported by the Singapore Ministry of Education Academic Research Fund Tier 2 under the Project No. MOE2015-T2-1-016 and the Singapore National Research Foundation under CRP Award No. NRF-CRP10-2012-02. Work at Brookhaven National Laboratory was supported by the U.S. Department of Energy, Office of Basic Energy Science, Division of Materials Science and Engineering, under Contract No. DESC0012704. PY is supported from SSLS via NUS Core Support C-380-003-003-001. Sector 20 facilities at the Advanced Photon Source, and research at these facilities, are supported by the US Department of Energy - Basic Energy Sciences, the Canadian Light Source and its funding partners, the University of Washington, and the Advanced Photon Source. Use of the Advanced Photon Source, an Office of Science User Facility operated for the U.S. Department of Energy (DOE) Office of Science by Argonne National Laboratory, was supported by the U.S. DOE under Contract No. DE-AC02-06CH11357.

References

1. S. J. May, *et. al*, *Nature Mater*. 8, 892 - 897 (2009).
2. J. Chakhalian, *et. al*, *Nature Phys.* 2, 244 - 248 (2006).
3. J. Chakhalian, *et al*, *Science* 318, 1114 - 1117 (2007).
4. A. Ohtomo, *et al*, *Nature* 427, 423 - 426 (2004).
5. *Qi Hang Qin, et. al*, *Adv.Mater*. 28, 6852–6859 (2016).
6. James M. Rondinelli *et. al*, *Adv.Mater.* 23, 3363 - 3381 (2011).
7. Hans Boschker, *et. al*, *Phys. Rev. Lett.*109, 157207 (2012).
8. Jun He, *et. al*, *Phys Rev Lett.*105, 227203 (2010).
9. Z. Wang et al, *Phys. Rev. B* 94 155307 (2016).
10. Ryotaro Aso, *et. al*, *Crystal Growth Design*, 14, 2128 (2014)
11. Liang Qiao *et. al, Nano Lett.,* 15, 4677 (2015).
12. E. J. Moon *et. al, Nano Lett.,* 14, 2509 (2014).
13. Bangmin Zhang, *et. al*, *Nano Lett.* 16, 4174 - 4180 (2016).
14. Z. Liao, *et al*, *Nature Mater.* 15, 425 - 431 (2016).
15. Daisuke. Kan, *et al*, *Nature Mater.* 15, 432 - 437 (2016).
16. Dagotto, E.; Hotta, T.; Moreo, A. *Phys. Rep.* 344, 1 (2001).
17. Yang Ding *et. al*, *Phys Rev Lett.*102, 237201 (2009).
18. Segal, Y. *et. al.*, *Phys Rev Lett.* 107, 105501, (2011).
19. S. Zhang *et. al*, *Phys Rev Lett.* 108, 137203 (2012).
20. Kyung-Min Ham *et. al*, *Phys. Rev. B* 50.16598 (1994).
21. Popović, Z., *et. al*, *Phys. Rev. Lett.* 101, 256801 (2008).
22. Javier Garcia-Barriocanal *et al. Adv. Mater.* 22, 627 - 632 (2010).
23. H. Kumigashira, *et al.* Appl. Phys. Lett. 84, 5353 (2004).
24. C A F Vaz, *et al.* J. Phys.: Condens. Matter 27, 123001 (2015).
25. Kim, M. S. *et. al*, *Phys. Rev. B* 71, 014433 (2005).
26. Loetzsch, R *et. al*, *Appl. Phys. Lett.* 96, 071901 (2010).
27. G. Shzrane, *et. al*, *Phys. Rev.* 177, 858-863 (1969).
28. M. Izumi *et. al*, *Phys. Rev. B*, 64, 064429 (2001).
29. M. C. Dekker *et. al*, *Phys. Rev. B* 84, 054463 (2011).
30. Xiaofang Zhai *et. al*, *Nat. Commu.* 5,4283 (2014).
31. C. Chen et al., *Phys. Rev. Lett.* 75, 152 (1995).
32. S. Ikeda *et al.*, *Nature Mater*. **9** 721 (2010).

33. Glazer, A. M. *Acta Crystallogr., Sect. B: Struct. Crystallogr. Cryst. Chem.* 28, 3384 (1972).
34. Woodward, P. M. *Acta Crystallogr., Sect. B: Struct. Sci.*, 53, 32 (1997).
35. Bangmin Zhang, *et. al*, *Phys. Rev. B* 89, 195140 (2014).
36. Martin J. Hÿtch, Jean-Luc Putaux, Jean-Michel Pénisson *Nature* 423, 270-273 (2003)
37. Lijun Wu *et. al*, J. Appl. Phys. 105, 094317 (2009).
38. Hanghui Chen *et. al*, *Nano Lett.* 14, 4965 (2014).
39. M. Dawber, *et. al*, *Phys. Rev. Lett.* 95, 177601 (2005).
40. E. STOYANOV *et al. Am. Mineral*, 92, 577 - 586 (2007).
41. Javier Garcia-Barriocanal *et al. Adv. Mater.* 22, 627 - 632 (2010).
42. M. Gibert *et al. Nano Lett.* 15, 7355 - 7361 (2015).
43. M. Varela *et al. Phys. Rev. B* 79, 085117 (2009).
44. D. Pesquera *et al. Nat. Commun* 3, 1189 (2012).
45. A. Tebano *et al. Phys. Rev. Lett.* 100, 137401 (2008).
46. Norbert Marcel Nemes *et al.*, *Adv. Mater*. 26, 7516 (2014).
47. Satoshi Okamoto, *Phys. Rev. B* 82, 024427 (2010).
48. J. Garcia-Barriocanal *et al.*, *Nat. Commun* 1, 82 (2010).
49. H. Tolentino, *et. al*, *Phys. Rev. B* 45, 8091 (1992).
50. You Zhou, *et. al*, *Natur*e 534, 231 - 234 (2016).
51. O. Bunau *et. al*, *J. Phys. : Condens. Matter* 21, 345501 (2009).

Figure 1

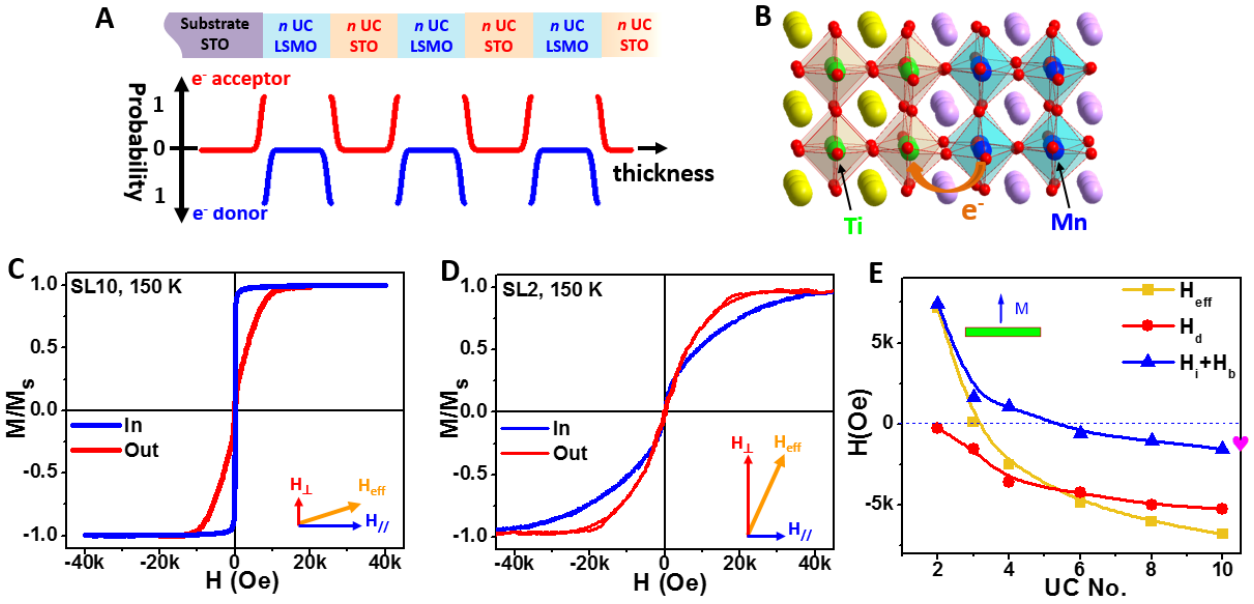

Figure 1: (**A**) Illustration of probability of electronic charge transfer at LSMO/STO interfaces, which occurs in length scale of a few unit cells; the probability is normalized to that at interface. The red line is the probability as electron acceptor, and the blue line is the probability as electron donor. (**B**) The illustration of charge transfer from Mn to Ti across the interface; (**C**-**D**) the magnetic hysteresis loop at 150 K for SL10 and SL2. The inset in each figure shows the effective anisotropy due to the sum of in-plane and out-of-plane magnetic anisotropy. (**E**) The summary of magnetic anisotropy for SL*n* at 150 K. $\boldsymbol{H}_{\mathrm{eff}}$ is the effective anisotropy field calculated from the hysteresis loop, $\boldsymbol{H}_{\mathrm{d}}$ is the demagnetization field, $\boldsymbol{H}_{\mathrm{i}}$ is the interfacial contribution to effective anisotropy field, and $\boldsymbol{H}_{\mathrm{b}}$ is the bulk term which is constant value for all samples. The pink heart (♥) on the right indicates the magnetic anisotropy of a single LSMO layer with thickness 60 unit cells on $SrTiO_3$ substrate.

Figure 2

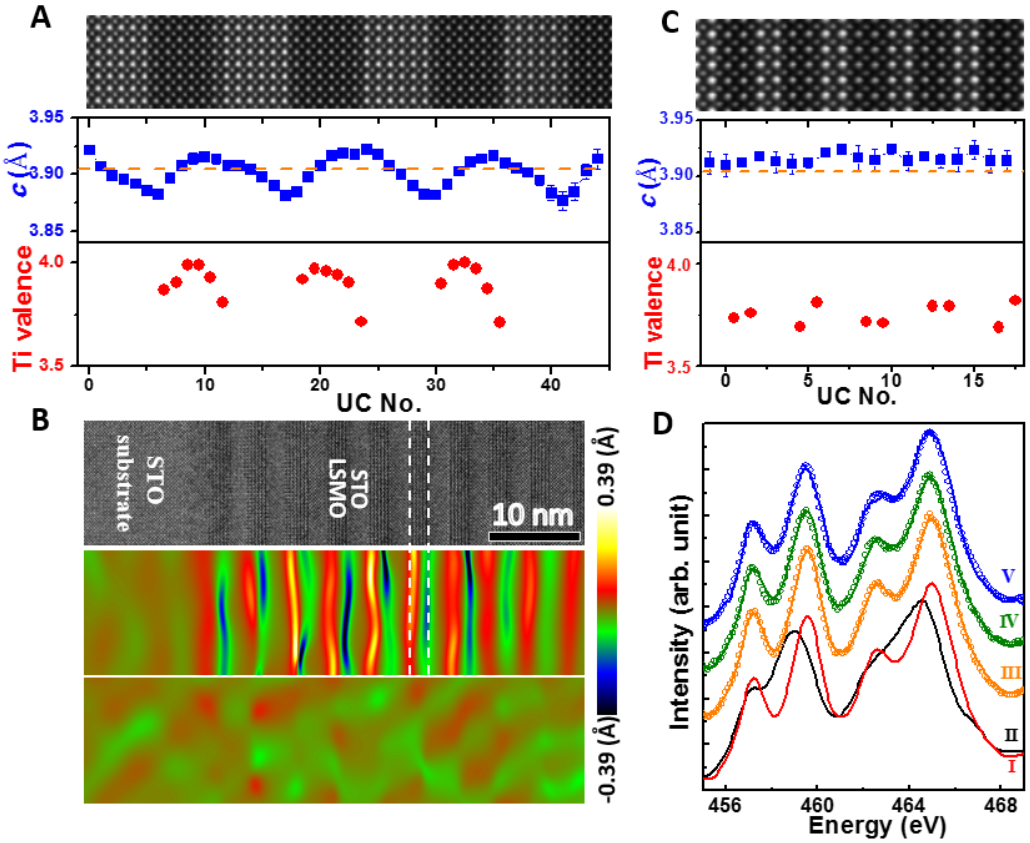

Figure 2: HAAD-STEM images of (**A**) SL6 and (**C**) SL2 LSMO/STO superlattice films. Out-of-plane plane spacing c_{int} (blue squares) and Ti chemical valence (red dots) as a function of position is shown in the middle and bottom part of **A & C**, respectively. The horizontal orange dashed lines mark the c_{int} of STO in substrate. (**B**) High resolution TEM (HRTEM) image from SL6. The second and third rows are corresponding relative change of out-of-plane (second row) and in-plane (third row) spacing of SrO (La/SrO) planes, calculated based on geometry phase analysis (GPA)[36-37] with the substrate STO as reference. The color scheme is shown in the middle. The vertical white dashed lines at two STO/STO interfaces are for eye guidance. Refers to **S8** for more details. (**D**) Ti EELS at $L_{3,2}$ edges from $SrTiO_3$ substrate far from interface (I: red line), sample surface (II: black line), interface between LSMO/STO superlattice (III: orange circles), center of deposited STO layer in LSMO/STO superlattice (VI: olive circles) in SL6, and deposited STO layer in SL2 film (V: blue circles). The spectra of I and II are close to those of bulk $SrTiO_3$ and $LaTiO_3$, respectively, thus used as the reference spectra of Ti^{4+} and Ti^{3+}. The orange, olive and blue solid lines are the corresponding fitting lines for the spectra of III-V

(circles) based on multiple linear least square (MLLS) fitting with the reference spectra of I and II. The fitting coefficients associated with spectrum I are 0.98, 0.82 and 0.81 for III, VI and V, respectively. The Ti valence can therefore be determined as Ti^{4+}, $Ti^{3.78+}$ and $Ti^{3.75+}$, respectively. Ti valence distribution obtained by multiple linear least square (MLLS) fitting of the EELS spectrum image is shown in bottom part of (**A & C**). More than 1000 spectra were collected over the scan line, and dozens of spectra around Ti atoms were then averaged for MLLS fitting.

Figure 3

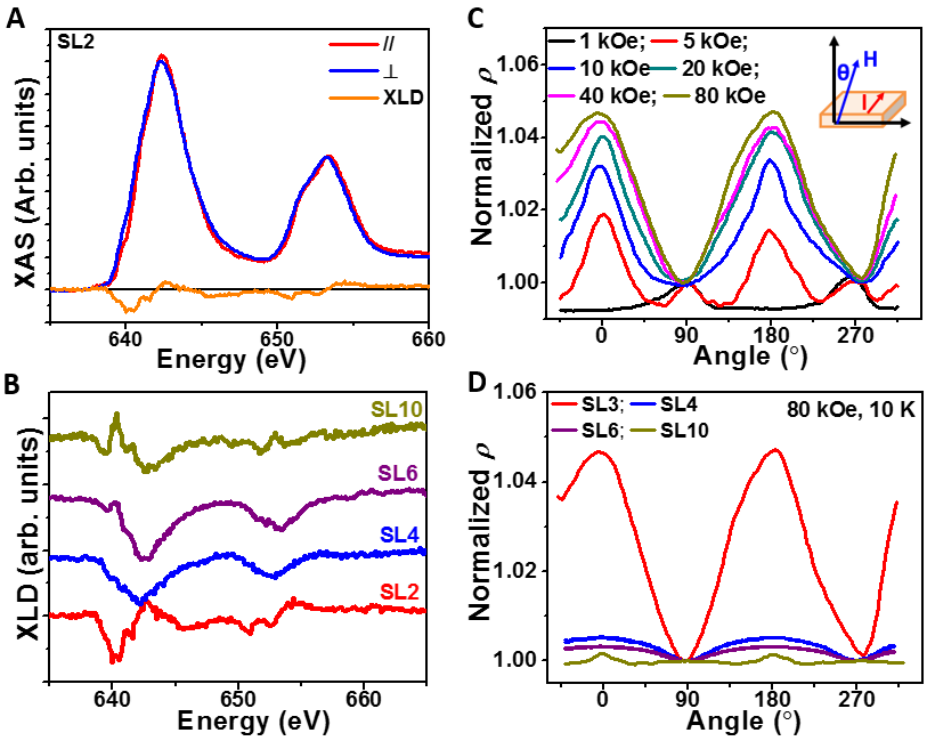

Figure 3: (**A**) The detailed XAS curves for n = 2, and the summarized ***L*** edge XLD for four samples is shown in (**B**); the parallel measurement (//, red) with electric field of X-ray in the film plane and perpendicular measurement (⊥, blue) with electric field perpendicular to the film plane. Larger absorption for parallel measurement indicates more in-plane empty states in the e_g band and higher occupancy of out-of-plane orbitals. **(C**) The effect of magnetic field on the angular dependence of magnetoresistance (AMR) of SL3. All curves are normalized to the resistance at θ = 0°. The measurement configuration is illustrated as the inset of (**C**); (**D**) Summary of AMR at 10 K with magnetic field of 80 kOe for different samples.

Figure 4

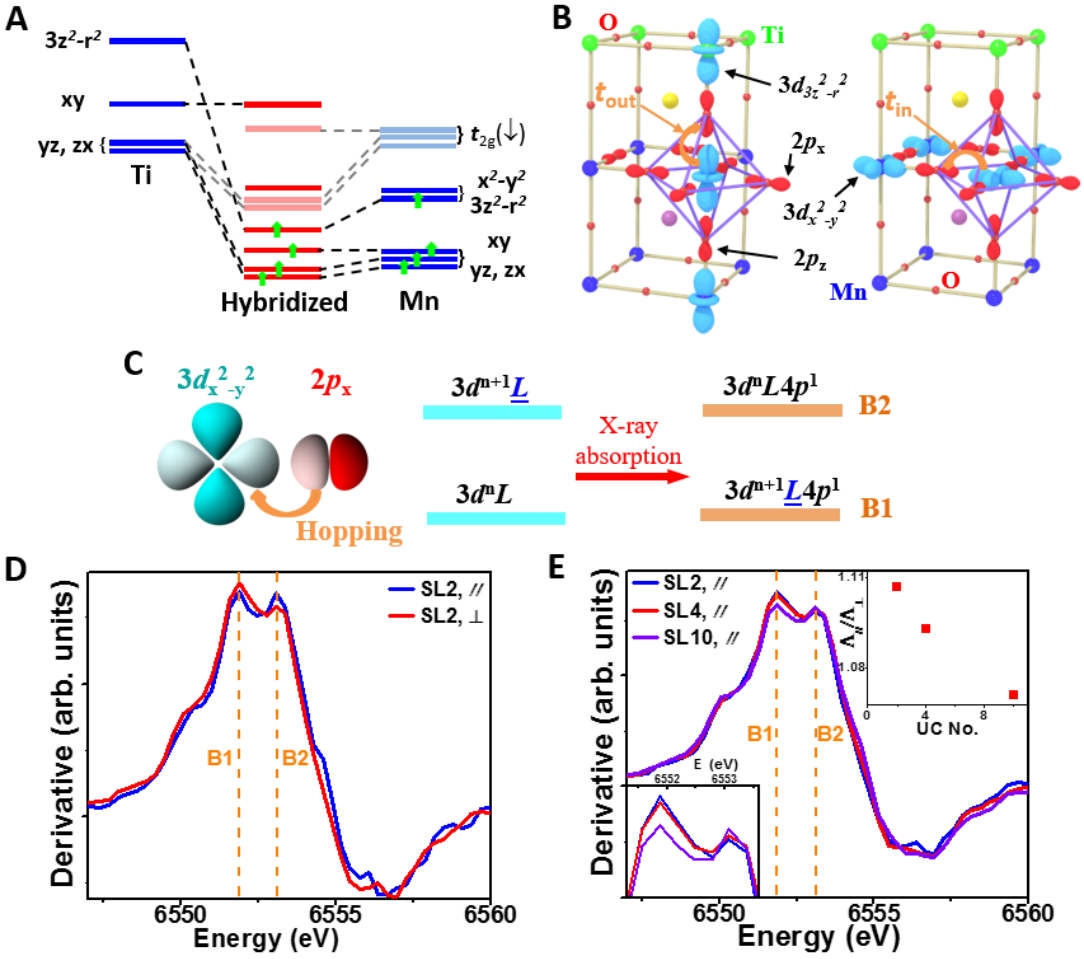

Figure 4: (**A**) The illustration of the 3*d* orbital energy levels after hybridization between Mn and Ti across the interface. More discussion in the text. (**B**) The illustration of electronic hopping along the in-plane integral ($\boldsymbol{t}_{in}$) through Mn $3\boldsymbol{d}_{x^2-y^2}$, and the out-of-plane ($\boldsymbol{t}_{out}$) direction through Mn $3\boldsymbol{d}_{3z^2-r^2}$. (**C**) The illustration of electronic configuration before and after X-ray absorption. The *L* denotes the six oxygen ligand around Mn, and $\underline{L}$ denotes one electron missing of the ligand, which locates at Mn site orbital orbitals through hopping between O $2\boldsymbol{p}_x$ or $2\boldsymbol{p}_y$ and Mn $3\boldsymbol{d}_{x^2-y^2}$ orbital. Similar would happen between O $2\boldsymbol{p}_z$ and Mn $3\boldsymbol{d}_{3z^2-r^2}$ orbital. See Refs. [35, 49-50] for more details. (**D**) The derivative of the polarization dependent Mn ***K*** edge XANES with the electric field of the X-ray parallel (//) and perpendicular (⊥) to the film plane. There are two features B1 and B2 at the ***K*** edge. The enhanced B1peak in the parallel configuration indicates the stronger electronic hopping integral along the out-of-plane direction. (**E**) The comparison of XAS for three samples in parallel configuration, which relates to the out-of-plane electronic

hopping integral $\boldsymbol{t}_{out}$; The lower inset is the enlarged part around B1 and B2 peaks; the upper inset indicates the trend of $\Lambda_{///}/\Lambda_{\perp}$. $\Lambda_{//}$ and $\Lambda_{\perp}$ indicate the I_{B1}/I_{B2} ratio in parallel and perpendicular configurations, respectively.